

Bridging the mid-infrared-to-telecom gap with silicon nanophotonic spectral translation

Xiaoping Liu^{1†‡}, Bart Kuyken^{2‡}, Gunther Roelkens², Roel Baets², Richard M. Osgood Jr¹ and William M. J. Green^{3*}

Extending beyond traditional telecom-band applications to optical interconnects¹, the silicon nanophotonic integrated circuit platform also has notable advantages for use in high-performance mid-infrared optical systems operating in the 2–8 μm spectral range^{2,3}. Such systems could find applications in industrial and environmental monitoring⁴, threat detection⁵, medical diagnostics⁶ and free-space communication⁷. Nevertheless, the advancement of chip-scale systems is impeded by the narrow-bandgap semiconductors traditionally used to detect mid-infrared photons. The cryogenic or multistage thermo-electric cooling required to suppress dark-current noise⁸, which is exponentially dependent on E_g/kT , can restrict the development of compact, low-power integrated mid-infrared systems. However, if the mid-infrared signals were spectrally translated to shorter wavelengths, wide-bandgap photodetectors could be used to eliminate prohibitive cooling requirements. Furthermore, such detectors typically have larger detectivity and bandwidth than their mid-infrared counterparts⁹. Here, we use efficient four-wave mixing in silicon nanophotonic wires^{9–12} to facilitate spectral translation of a signal at 2,440 nm to the telecom band at 1,620 nm, across a span of 62 THz. Furthermore, a simultaneous parametric translation gain of 19 dB can significantly boost sensitivity to weak mid-infrared signals.

The silicon spectral translator device is capable of performing the complementary function of a mid-infrared transmitter, converting telecom-band signals to the mid-infrared with a translation gain of 8.0 dB. Finally, this device also demonstrates an optical parametric amplification of 8.4 dB for telecom-band input signals, reinforcing the wide-ranging technological role silicon nanophotonic wires can play within both mid-infrared and telecom bands.

Spectral translators making use of sum- or difference-frequency generation in nonlinear crystals (including LiNbO_3 ^{13,14} and KTP ¹⁵) have been studied previously. However, such systems can be limited by low conversion efficiencies, their significant size and the limited integrability of their component parts. These challenges are addressed by the silicon nanophotonic spectral translator explored here, which can be integrated easily with the numerous mid-infrared silicon components demonstrated to date, including waveguides^{16–18}, vertical grating couplers¹⁹, microcavities^{20,21} and electrooptic modulators²².

Mid-infrared to telecom-band spectral translation in silicon nanophotonic wires is accomplished using efficient four-wave mixing (FWM) with discrete band phase-matching^{23,24}. In this process, the pump is placed away from the zero dispersion wavelength, and higher-order waveguide dispersion is used to

phase-match a discrete pair of bands at spectrally distant frequencies, located symmetrically on either side of the pump. Discrete band phase-matching can be achieved in a waveguide with anomalous second-order dispersion ($\beta_2 < 0$) and small positive fourth-order dispersion ($\beta_4 > 0$) (Supplementary Fig. S1), conditions that are engineered¹¹ by manipulating the cross-sectional dimensions and cladding materials of the silicon nanophotonic wire. Figure 1a presents an optical microscope image of the 2-cm-long silicon nanophotonic wire used here for spectral translation, which was fabricated on a 200 mm silicon-on-insulator (SOI) wafer (at imec) using the multi-project-wafer service ePIXfab (www.ePIXfab.eu). The entire length of the wire is coiled into a compact spiral, occupying an on-chip footprint of only $625 \mu\text{m} \times 340 \mu\text{m}$. The wire has cross-sectional dimensions of $w = 900 \text{ nm}$ and $h = 220 \text{ nm}$ (Fig. 1b). The cladding consists of air above and a $2 \mu\text{m}$ buried oxide (SiO_2) below the silicon core. Numerical simulations indicate that the dispersion conditions $\beta_2 < 0$ and $\beta_4 > 0$ are satisfied over the spectral range 1,810–2,410 nm (Supplementary Fig. S2). Over a similar range, a large effective nonlinearity parameter of $114 \leq \gamma \leq 276 \text{ W}^{-1} \text{ m}^{-1}$ and a low propagation loss of 2.6 dB cm^{-1} also serve to facilitate highly efficient FWM for this compact device.

The nonlinear mixing and spectral translation characteristics of the silicon nanophotonic wire are presented in Fig. 1c,d. Figure 1c shows the recorded output spectrum when the wire is excited by a pump pulse train at 1,946 nm with a peak coupled input power of 37.3 W (for experimental details see Methods). While this pump wavelength is not yet beyond silicon's two-photon absorption (TPA) threshold of 2,200 nm (ref. 25), the TPA coefficient is nevertheless a factor of 2 to 3 lower than that at 1,550 nm, resulting in small nonlinear loss and efficient FWM. For example, in the absence of any probe signal (signal OFF), the pump transmission spectrum already exhibits clear signatures of the desired phase-matched FWM processes. Specifically, strong broadband modulation instability (MI) peaks¹² appear adjacent to the pump at 1,810 nm and 2,090 nm. Moreover, two additional discrete MI bands with much larger detuning from the pump appear at 1,620 nm and 2,440 nm, and serve as direct evidence of higher-order phase-matching. The absolute power of the MI band at 2,440 nm appears lower than that of the MI band at 1,620 nm, due to a 1.8 dB asymmetry expected from the Manley–Rowe power division relations, as well as from ~ 3 – 4 dB larger losses in the output fibre optical collection path at longer wavelengths.

The visibility of the MI bands, associated with the parametric amplification of background noise, suggests that the pumped silicon nanophotonic wire should exhibit significant parametric

¹Department of Electrical Engineering, Columbia University, 1300 SW Mudd Building, 500 W. 120th Street, New York 10027, USA, ²Photonics Research Group, Department of Information Technology, Ghent University–Imec, Ghent B-9000, Belgium, ³IBM T. J. Watson Research Center, Yorktown Heights, New York 10598, USA; [†]Present address: OFS Labs, 19 Schoolhouse Road, Somerset, New Jersey 08873, USA; [‡]These authors contributed equally to this work. *e-mail: wgreen@us.ibm.com

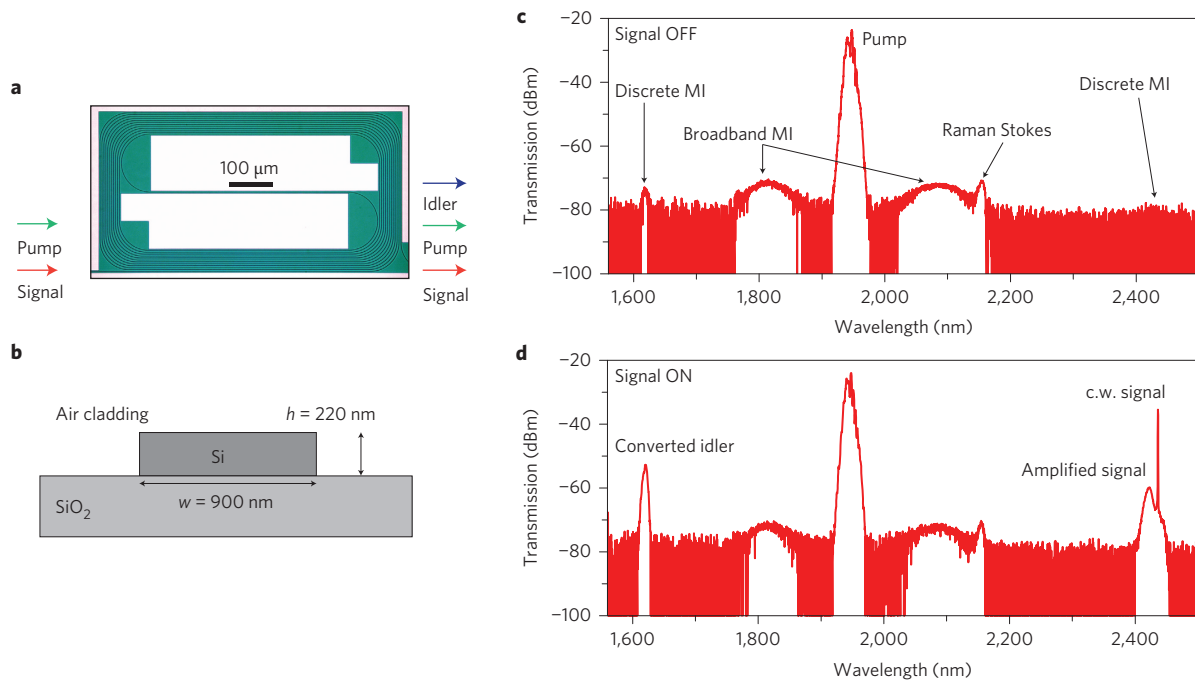


Figure 1 | Structural design and transmission characteristics of the silicon nanophotonic wire spectral translation device. a, Optical microscope image of the spiral-coiled silicon wire (total length, 2 cm; on-chip footprint, $625 \mu\text{m} \times 340 \mu\text{m}$). Bends with a conservative $60 \mu\text{m}$ radius are used. Arrows depicting the pump, signal and idler beams illustrate the input/output experimental configuration. **b**, Cross-sectional schematic, illustrating a silicon core (width, $w = 900 \text{ nm}$; height, $h = 220 \text{ nm}$), which lies on a $2\text{-}\mu\text{m}$ -thick SiO_2 buried oxide layer. The silicon core is air-clad from above. **c**, Output transmission spectrum with pump operating at $\lambda = 1,946 \text{ nm}$ and input signal OFF. The observed modulation instability spectrum generated by amplification of background noise serves as a marker of the spectral bands in which phase-matching conditions are met. The location of the broadband MI peaks adjacent to the pump at $1,810 \text{ nm}$ and $2,090 \text{ nm}$ is primarily determined by β_2 , while the discrete MI bands at $1,620 \text{ nm}$ and $2,440 \text{ nm}$ occur as a result of higher-order phase-matching dictated by the values of both β_2 and β_4 . A Raman Stokes peak is also observed at $2,155 \text{ nm}$. **d**, Transmission spectrum with input signal ON. A c.w. mid-infrared signal is tuned to coincide with the discrete MI band at $2,440 \text{ nm}$. Parametric amplification of the signal occurs, with simultaneous spectral translation across 62 THz , to an idler at $1,620 \text{ nm}$.

gain as well as large conversion efficiency when probed by input signals at these wavelengths. Figure 1d illustrates the output spectrum in one such case, when the long-wavelength discrete MI band is probed (signal ON) by a low-power ($P_{\text{sig}} < 35 \mu\text{W}$) continuous-wave (c.w.) mid-infrared signal at $2,440 \text{ nm}$. When the signal is tuned into resonance with this spectral band, it experiences strong parametric amplification through degenerate FWM (evidenced by the appearance of the large spectral pedestal), and is simultaneously upconverted to a prominent telecom-band idler at $1,620 \text{ nm}$. Analysis of the output spectrum (see Methods) reveals that the peak on-chip powers of the amplified signal and the converted idler are 1.7 mW and 2.0 mW , respectively. The large spectral translation over more than 62 THz illustrates that the higher-order dispersion design methodology applied here may be used to efficiently convert optical information on a mid-infrared carrier into the telecom band, where it can be detected and processed using uncooled, high-speed, high-sensitivity groups III–V (InGaAs) and group IV (germanium) semiconductor detector technologies.

By recording transmission spectra for a range of signal wavelengths near $2,440 \text{ nm}$ and $1,620 \text{ nm}$, the wavelength dependence of spectral translation efficiency and parametric gain within the discrete phase-matching bands can be determined (see Methods). Figure 2a illustrates that, for mid-infrared input signals, the silicon wire device attains optical transparency (on-chip gain exceeding 0 dB) across a bandwidth of 150 nm near the signal and 45 nm near the idler. The data also demonstrate that spectral translation of mid-infrared signals to the telecom-band idler near $1,620 \text{ nm}$ takes place with a peak conversion gain of 19.5 dB .

Therefore, not only could such a spectral translator facilitate detection of mid-infrared signals without cumbersome cooling requirements, the associated optical gain could also dramatically improve the sensitivity of such a receiver system, particularly for weak mid-infrared input levels²⁶. At the same time, the mid-infrared input signal experiences a peak on-chip parametric amplification of 18.8 dB .

Figure 2b shows the results for a similar set of experiments, in which a telecom-band input signal is tuned across the MI peak near $1,620 \text{ nm}$. In this case, the on-chip transparency bandwidth is $\sim 20 \text{ nm}$ for the signal and 40 nm for the idler. The telecom-band signal is spectrally translated to the mid-infrared with a peak gain of 8.0 dB . If the telecom-band input is amplitude- or phase-modulated, the spectral translation process can be used to generate format-preserved mid-infrared signals using commercially available telecom components^{27,28}. In addition to performing the spectral translation function, Fig. 2b illustrates that the telecom-band input signal is simultaneously amplified by 8.4 dB . The demonstration of a silicon wire amplifier that uses a mid-infrared pump to provide substantial parametric gain to a telecom-band signal is of particular technological significance, as such an amplifier could find applications within the CMOS-integrated silicon nanophotonic platforms currently being developed for high-speed optical interconnect systems¹.

The spectral translation of the telecom-band signal to the mid-infrared shown in Fig. 2b occurs with an $\sim 11 \text{ dB}$ gain reduction when compared with the reversed scenario illustrated in Fig. 2a. As the energetic combination of a $1,620 \text{ nm}$ signal photon with a pump photon lies significantly above the bandgap of silicon, the

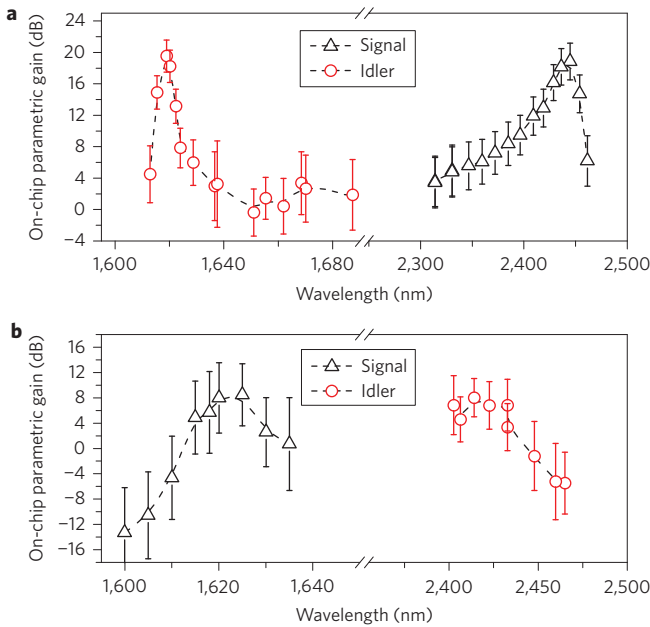


Figure 2 | Wavelength-resolved on-chip spectral translation efficiency and parametric signal gain. **a**, Injection of a mid-infrared input signal ($P_{sig} < 35 \mu W$), with translation to a telecom-band output idler. The peak on-chip translation efficiency is 19.5 dB, and the signal gain is 18.8 dB. The transparency bandwidth exceeds 45 nm near the idler, and 150 nm near the signal. **b**, Reversed scenario, with injection of a telecom-band input signal ($P_{sig} < 50 \mu W$) and translation to a mid-infrared output idler. The peak on-chip translation efficiency is 8.0 dB, and the signal gain is 8.4 dB. Transparency is reached over a bandwidth of 40 nm near the idler and 20 nm near the signal. In all of the above measurements, the silicon nanophotonic wire is pumped at 1,946 nm with a peak power of 37.3 W. The small shift in the spectral position of the mid-infrared gain peak between **a** and **b** (2,440 nm versus 2,420 nm, respectively) occurs as a result of pump wavelength drift. The dashed curves are included as a guide to the eye. Estimation of error bars is described in the Supplementary Methods.

observed asymmetry is expected due to the effects of non-degenerate TPA^{23,25} in the silicon wire. Non-degenerate TPA produces greater attenuation in an input signal near 1,620 nm than in one near 2,440 nm when each is combined with the strong pump at 1,946 nm. Therefore, larger gain values could be expected for the telecom-band signal if the pump wavelength were increased.

The phase-matched signal and idler wavelengths linked by the discrete FWM spectral translation process are dependent on the magnitudes of β_2 and β_4 , and can therefore be tuned by selection of the wavelength at which the dispersive silicon nanophotonic wire is pumped. The spectral separation between bands is expected to increase for large values of $|\beta_2|$ and small values of $|\beta_4|$. Figure 3a plots the spectral locations at which the discrete signal and idler MI bands appear as a function of the pump wavelength. The figure illustrates that the bands are maximally separated by 865 nm when the wire is pumped at 1,998 nm. Conversely, the bands are observed to move closer together as the pump approaches the two zero-group velocity dispersion (GVD) points located at 1,810 nm and 2,410 nm.

An optimization of the silicon nanophotonic wire dispersion design, focusing on increasing $|\beta_2|$ while simultaneously decreasing $|\beta_4|$, can facilitate the translation of even longer-wavelength mid-infrared signals into the telecom band. For example, Fig. 3b plots numerical calculations of the phase-matched discrete signal and idler wavelengths of a design tailored for translating a range of mid-infrared signals from 3,000 to 3,550 nm into the L-band (see Methods). This spectrum is targeted for its overlap with a

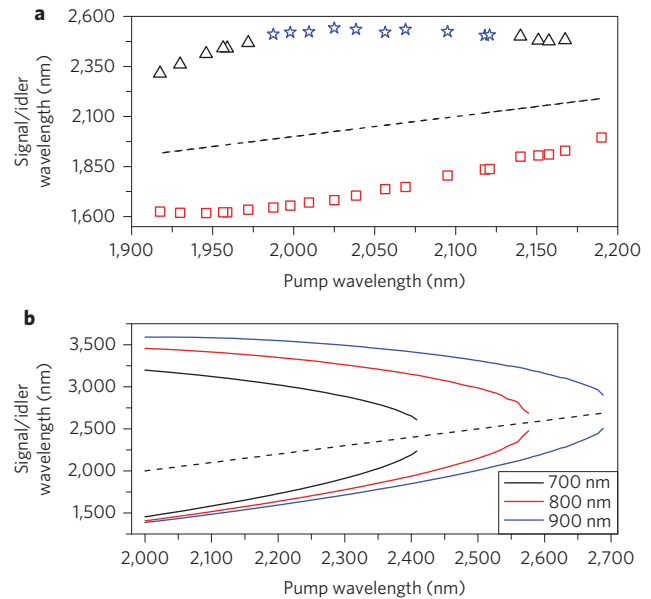


Figure 3 | Phase-matched signal and idler wavelengths linked by the silicon nonphotonic spectral translation process. **a**, Symbols mark the spectral locations of the discrete MI bands as a function of pump wavelength, for the experimentally demonstrated silicon wire ($w = 900$ nm, $h = 220$ nm). The MI bands indicated by blue stars were not measured directly, as they were located beyond the 2,500 nm maximum wavelength limit of the spectrum analyser used. The positions of these bands were therefore inferred from energy conservation. **b**, Design calculations describing the phase-matched discrete band locations versus pump wavelength, for the fundamental quasi-TE mode of an SiO_2 -clad silicon wire ($h = 300$ nm; $w = 700$ nm, 800 nm and 900 nm). The wires are tailored for spectral translation across more than an octave in optical frequency, between the 3,000–3,550 nm mid-infrared range and the L-band. The calculations assume c.w. pumping with 300 mW pump power. In both panels, the dashed line marks the pump wavelength.

mid-infrared low-loss window in SiO_2 (ref. 2). This design consists of a silicon wire with a thickness of 300 nm and a width in the range 700–900 nm, completely surrounded by an oxide cladding (Supplementary Fig. S4). In the specific case of a wire with $w = 900$ nm and $h = 300$ nm, Fig. 3b illustrates that an input signal at 3,550 nm could be spectrally translated to an L-band idler at 1,590 nm (and vice versa), using a pump wavelength of 2,200 nm. This corresponds to a span of 104 THz, more than an octave in optical frequency.

Moreover, although a pulsed pump with a high peak power is used in the present demonstration, a practical spectral translation system will require a c.w. pump to eliminate any requirement for synchronization of the input mid-infrared signals to the pump repetition period. Because the dispersion characteristics of the oxide-clad wire were designed with the intent of operating the pump at or beyond the TPA threshold of silicon at 2,200 nm, c.w. parametric gain is made possible by avoiding the deleterious effects of nonlinear loss and TPA-induced free-carrier absorption. Detailed calculations described in the Supplementary Methods and plotted in Supplementary Fig. S5 show that c.w. spectral translation of a 3,550 nm input signal to 1,590 nm can be accompanied by a translation gain as large as 22 dB for a moderate pump power of 300 mW at 2,200 nm.

Finally, the performance of silicon nanophotonic spectral translation can be compared to conventional direct photodetection by means of their respective electrical signal-to-noise ratios²⁶ (eSNRs). Considering specifically the pulsed experimental

demonstration in Fig. 1d, a noise analysis suggests (Supplementary Methods) that the eSNR resulting from direct detection at 2,440 nm can exceed the eSNR of spectral translation with detection at 1,620 nm by a nominal 1.6 dB. Depending on the application, a small eSNR penalty may be an acceptable trade-off to leverage the distinct advantages of mid-infrared detection via spectral translation, which include uncooled operation and therefore smaller, lighter, more highly integrated mid-infrared optical systems. On the other hand, analogous noise estimates made for the c.w. pumped case (Supplementary Methods and Supplementary Fig. 6c) reveal that spectral translation can substantially outperform the eSNR of traditional direct detection by as much as 17 dB for a pump power of 150 mW, while simultaneously consuming as little as 25% of the electrical power.

In summary, we have shown that judicious engineering of FWM processes in silicon nanophotonic wires can facilitate amplified bidirectional spectral translation of signals between the mid-infrared and the telecom band, across a 62 THz span in optical frequency. Telecom-band detection of translated mid-infrared signals can eliminate the burdensome cooling requirements traditionally associated with mid-infrared photodetectors, and can be performed by on-chip photodetectors integrated via heterogeneous²⁹ or monolithic³⁰ techniques. Moreover, these spectral translation devices can be integrated (Supplementary Fig. S7) with additional mid-infrared and/or telecom-band silicon nanophotonic components such as modulators, wavelength (de-)multiplexers and switches, which together have the potential to produce flexible, chip-scale optical systems for mid-infrared applications.

Methods

FWM experimental configuration. In the present set-up the FWM pump is a picosecond pulse train (full-width at half-maximum (FWHM), ~ 2 ps; repetition rate, 76 MHz) from a tunable optical parametric oscillator (mode-locked Ti:sapphire-pumped Coherent Mira-OPO). The pump spectrum has a signal-to-noise ratio larger than 70 dB over the wavelength range 1,600–2,500 nm (Supplementary Fig. S3). The c.w. probe signals are obtained either from a tunable mid-infrared laser (IPG Photonics SFTL Cr²⁺:ZnSe polycrystal with erbium-fibre laser pump source) or a tunable telecom laser (Agilent 81640A). Pump and probe are coupled into two separate single-mode optical fibres, aligned individually with polarization controllers to excite the fundamental quasi-transverse electric (TE) mode in the silicon nanophotonic wire, and then multiplexed with a 90/10 fused fibre directional coupler. Coupling into/out of the 2-cm-long silicon nanophotonic wire is accomplished via cleaved facet edge coupling with lensed tapered fibres (coupling losses = 10 ± 1 dB/facet, across the entire spectral range utilized). The spectral content of the transmitted light is analysed with 1 nm spectral resolution, using a mid-infrared optical spectrum analyser (OSA, Yokogawa AQ6375).

Extraction of spectral translation efficiency and signal gain. The peak power of the spectrally translated idler pulse at the output of the silicon nanophotonic wire, $P_{\text{idler, out}}$, was derived from the measured FWM spectra according to $P_{\text{idler, out}} = F \int P_{\text{idler, avg}}(\lambda) d\lambda$. To convert the time-averaged idler power $P_{\text{idler, avg}}$ measured by the OSA into peak power, the spectrally integrated power was weighted by the duty cycle factor $F = 1/(76 \text{ MHz} \cdot 2 \text{ ps})$ to account for the pulsed nature of the experiment. A similar procedure was applied to calculate the signal output power $P_{\text{signal, out}}$. A 2-nm-wide band-stop filter was first numerically applied to the time-averaged signal spectrum to reject the power remaining in the narrowband c.w. tone. The peak signal power was then computed according to $P_{\text{signal, out}} = F \int P_{\text{signal, filtered, avg}}(\lambda) d\lambda$. Finally, to find the c.w. signal power at the waveguide input $P_{\text{signal, in}}$, the output c.w. signal power was measured (with the pump off) and corrected to account for total propagation losses of α dB incurred through the 2-cm-long device, $P_{\text{signal, in}} = 10^{\alpha/10} \int P_{\text{signal, out, pump, off}}(\lambda) d\lambda$. The on-chip idler spectral translation gain η was then defined as the ratio of peak idler power and input c.w. signal power, $\eta = P_{\text{idler, out}}/P_{\text{signal, in}}$. Accordingly, the on-chip parametric signal gain is given by $G = P_{\text{signal, out}}/P_{\text{signal, in}}$. The error bars in the on-chip parametric gain data are calculated to reflect the uncertainty in the total propagation loss α , as well as the contribution of the MI noise background accumulated when integrating the signal/idler power at the waveguide output. Additional detail on the estimation of error bars is included in the Supplementary Methods.

Numerical calculations of signal and idler discrete band tuning versus pump wavelength. The linear phase-mismatch Δk_1 is characterized by $\Delta k_1 = \beta_s + \beta_i - 2\beta_p$, where β_s , β_i and β_p are the modal propagation constants for signal, idler and pump, respectively. These propagation constants and their spectral dispersion were obtained through numerical simulations using a commercial finite-element

eigen-mode solver (RSoft FemSim). Solving the phase-matching equation $\Delta k_1 + 2\gamma P = 0$ ($P = 300$ mW is assumed for the calculation in Fig. 3b) with signal and idler frequencies constrained by the pump detuning $\Delta\omega = |\omega_p - \omega_s| = |\omega_p - \omega_i|$ will generally yield two solutions for $\Delta\omega$. The smaller-valued solution corresponds to broadband phase-matched signal–idler regions appearing immediately adjacent to the pump, and is ignored for the purposes of spectral translation in this work. The larger-valued of the two solutions describes the discrete signal and idler bands appearing at large pump detuning. The curves of phase-matched signal–idler pairs shown in Fig. 3b were found by repeating this calculation for a range of pump frequencies, and converting to detuning in units of wavelength.

Received 8 April 2012; accepted 10 August 2012;
published online 23 September 2012

References

- Green, W. M. J. *et al.* in SEMICON (Chiba, 2010); available at www.research.ibm.com/photronics.
- Soref, R. Mid-infrared photonics in silicon and germanium. *Nature Photon.* **4**, 495–497 (2010).
- Jalali, B. *et al.* Prospects for silicon mid-IR Raman lasers. *IEEE J. Sel. Top. Quantum Electron.* **12**, 1618–1627 (2006).
- Willer, U., Saraji, M., Khorsandi, A., Geiser, P. & Schade, W. Near- and mid-infrared laser monitoring of industrial processes, environment and security applications. *Opt. Laser Eng.* **44**, 699–710 (2006).
- Moore, D. S. Instrumentation for trace detection of high explosives. *Rev. Sci. Instrum.* **75**, 2499–2512 (2004).
- Namjou, K., Roller, C. B. & McCann, P. J. The Breathmeter: a new laser device to analyze your health. *IEEE Circ. Dev. Magazine* 22–28 (2006).
- Capasso, F. *et al.* Quantum cascade lasers: ultrahigh-speed operation, optical wireless communication, narrow linewidth, and far-infrared emission. *IEEE J. Quantum Electron.* **38**, 511–532 (2002).
- Sze, S. M. *Physics of Semiconductor Devices* (Wiley, 1981).
- Zlatanovic, S. *et al.* Mid-infrared wavelength conversion in silicon waveguides using ultracompact telecom-band-derived pump source. *Nature Photon.* **4**, 561–564 (2010).
- Lau, R. K. W. *et al.* Continuous-wave mid-infrared frequency conversion in silicon nanowaveguides. *Opt. Lett.* **36**, 1263–1265 (2011).
- Liu, X., Osgood, J. R. M., Vlasov, Y. A. & Green, W. M. J. Mid-infrared optical parametric amplifier using silicon nanophotonic waveguides. *Nature Photon.* **4**, 557–560 (2010).
- Kuyken, B. *et al.* 50 dB parametric on-chip gain in silicon photonic wires. *Opt. Lett.* **36**, 4401–4403 (2011).
- Midwinter, J. E. & Warner, J. Up-conversion of near infrared to visible radiation in lithium-meta-niobate. *J. Appl. Phys.* **38**, 519–523 (1967).
- Buchter, K. D. F., Herrmann, H., Langrock, C., Fejer, M. M. & Sohler, W. All-optical Ti:PPLN wavelength conversion modules for free-space optical transmission links in the mid-infrared. *Opt. Lett.* **34**, 470–472 (2009).
- Dam, J. S., Pedersen, C. & Tidemand-Lichtenberg, P. High-resolution two-dimensional image upconversion of incoherent light. *Opt. Lett.* **35**, 3796–3798 (2010).
- Baehr-Jones, T. *et al.* Silicon-on-sapphire integrated waveguides for the mid-infrared. *Opt. Express* **18**, 12127–12135 (2010).
- Mashanovich, G. Z. *et al.* Low loss silicon waveguides for the mid-infrared. *Opt. Express* **19**, 7112–7119 (2011).
- Li, F. *et al.* Low propagation loss silicon-on-sapphire waveguides for the mid-infrared. *Opt. Express* **19**, 15212–15220 (2011).
- Kuyken, B. *et al.* in *Integrated Photonics Research*, paper IMB6 (Ottawa, 2011).
- Spott, A., Liu, Y., Baehr-Jones, T., Ilic, R. & Hochberg, M. Silicon waveguides and ring resonators at 5.5 μm . *Appl. Phys. Lett.* **97**, 213501 (2010).
- Shankar, R., Leijssen, R., Bulu, I. & Lončar, M. Mid-infrared photonic crystal cavities in silicon. *Opt. Express* **19**, 5579–5586 (2011).
- Van Camp, M. A. *et al.* in Conference on Lasers and Electro-Optics, paper CTu3I.2 (San Jose, 2012).
- Lin, Q., Johnson, T. J., Perahia, R., Michael, C. P. & Painter, O. J. A proposal for highly tunable optical parametric oscillation in silicon micro-resonators. *Opt. Express* **16**, 10596–10610 (2008).
- Tien, E. K. *et al.* Discrete parametric band conversion in silicon for mid-infrared applications. *Opt. Express* **18**, 21981–21989 (2010).
- Bristow, A. D., Rotenberg, N. & van Driel, H. M. Two-photon absorption and Kerr coefficients of silicon for 850–2200 nm. *Appl. Phys. Lett.* **90**, 191104 (2007).
- Huang, Y. *et al.* Electrical signal-to-noise ratio improvement in indirect detection of mid-IR signals by wavelength conversion in silicon-on-sapphire waveguides. *Appl. Phys. Lett.* **99**, 181122 (2011).
- Zlatanovic, S. *et al.* Mid-infrared wavelength conversion in silicon waveguides pumped by silica-fiber-based source. *IEEE J. Sel. Top. Quantum Electron.* **18**, 612–620 (2012).
- Ophir, N. *et al.* First demonstration of a 10-Gb/s RZ end-to-end four-wave-mixing based link at 1884 nm using silicon nanowaveguides. *IEEE Photon. Technol. Lett.* **24**, 276–278 (2012).

29. Roelkens, G. *et al.* Integration of InP/InGaAsP photodetectors onto silicon-on-insulator waveguide circuits. *Opt. Express* **13**, 10102–10108 (2005).
30. Assefa, S. *et al.* CMOS-integrated high-speed MSM germanium waveguide photodetector. *Opt. Express* **18**, 4986–4999 (2010).

Acknowledgements

The authors thank the staff at imec (Leuven, Belgium) where the silicon nanophotonic waveguide devices were fabricated. The authors also thank Y.A. Vlasov (IBM Research) for many helpful and motivating discussions. B.K. acknowledges the Flemish Research Foundation (FWO) for a doctoral fellowship. This work was partially funded under the Methusalem 'Smart Photonic Chips' FP7-ERC-INSPECTRA and FP7-ERC-MIRACLE programmes.

Author contributions

X.L. and B.K. performed the numerical dispersion and phase-matching design calculations. B.K., G.R. and R.B. supervised the waveguide device fabrication process. X.L. and B.K. performed the wavelength translation experiments with guidance and supervision from W.M.J.G. All authors contributed to data analysis and writing of the manuscript.

Additional information

Supplementary information is available in the online version of the paper. Reprints and permission information is available online at <http://www.nature.com/reprints>. Correspondence and requests for materials should be addressed to W.M.J.G.

Competing financial interests

The authors declare no competing financial interests.